Three-dimensional architecture of murine rod outer segments determined by cryoelectron tomography

Stephan Nickell,[1] Paul S.-H. Park,[2] Wolfgang Baumeister,[1] and Krzysztof Palczewski[2]

[1]Department of Molecular Structural Biology, Max Planck Institute of Biochemistry, D-82152 Martinsried, Germany
[2]Department of Pharmacology, School of Medicine, Case Western Reserve University, Cleveland, OH 44106

The rod outer segment (ROS) of photoreceptor cells houses all components necessary for phototransduction, a set of biochemical reactions that amplify and propagate a light signal. Theoretical approaches to quantify this process require precise information about the physical boundaries of the ROS. Dimensions of internal structures within the ROS of mammalian species have yet to be determined with the precision required for quantitative considerations. Cryoelectron tomography was utilized to obtain reliable three-dimensional morphological information about this important structure from murine retina. Vitrification of samples permitted imaging of the ROS in a minimally perturbed manner and the preservation of substructures. Tomograms revealed the characteristic highly organized arrangement of disc membranes stacked on top of one another with a surrounding plasma membrane. Distances among the various membrane components of the ROS were measured to define the space available for phototransduction to occur. Reconstruction of segments of the ROS from single-axis tilt series images provided a glimpse into the three-dimensional architecture of this highly differentiated neuron. The reconstructions revealed spacers that likely maintain the proper distance between adjacent discs and between discs and the plasma membrane. Spacers were found distributed throughout the discs, including regions that are distant from the rim region of discs.

Introduction

The venue for phototransduction, the process whereby a light stimulus is translated biochemically into an electrical signal, is the outer segment of rod and cone photoreceptor cells. Rods are highly differentiated cells with a cylindrical rod outer segment (ROS; Fig. 1). The ROS contains all components necessary for phototransduction and presents a remarkably well-ordered system of membranes. A ROS is composed of stacks of up to 2,000 discs surrounded by a plasma membrane (Daemen, 1973). The discs are shaped like flattened sacks that are made up of two lamellar membranes circumscribed by a hairpin rim region. Phototransduction is initiated in the discs by the absorption of a photon by rhodopsin and culminates in the closure of cyclic guanosine monophosphate–dependent ion channels located in the plasma membrane (Polans et al., 1996; Arshavsky et al., 2002). Whereas the integrity of the highly ordered structure of the ROS is critical to the fidelity of this signaling process, little is known about how this organization is maintained.

S. Nickell and P.S.-H. Park contributed equally to this paper.

Correspondence to Wolfgang Baumeister: baumeist@biochem.mpg.de

Abbreviations used in this paper: AFM, atomic force microscopy; ET, electron tomography; GARP, glutamic acid–rich protein; ROS; rod outer segment; TEM, transmission EM.

The online version of this contains supplemental material.

Changes in the structure of the ROS can lead to retinal dystrophies. Mouse models have provided many insights into understanding phototransduction and retinal dystrophies. Many mouse strains are available with naturally occurring mutations that lead to retinal dystrophies like *rd* and *rds* mice (for reviews see Chang et al., 2002; Dalke and Graw, 2005). Models of human retinal dystrophies have been created by genetic engineering in the form of transgenics, knockout, and knock-in methodologies (Dejneka et al., 2003). Moreover, mouse models of retinal dystrophies provide a method for testing various genetic and pharmacological therapies to combat diseases leading to blindness (Batten et al., 2005). Detailed morphological information from the native ROS, particularly from mice, will be important to understand mechanisms underlying phototransduction and retinal dystrophies.

EM studies have contributed substantially to our current understanding of the ROS structure. One of the earliest EM studies on the ROS was performed by Sjöstrand (1949) on samples from guinea pig. The most extensively studied ROS system comes from amphibian sources. EM studies have revealed conserved features of the ROS among vertebrates (Fig. 1 b; Daemen, 1973), which are likely to share similar mechanisms for structure maintenance. EM studies have also revealed differences

The Journal of Cell Biology, Vol. 177, No. 5, June 04, 2007 917–925
http://www.jcb.org/cgi/doi/10.1083/jcb.200612010

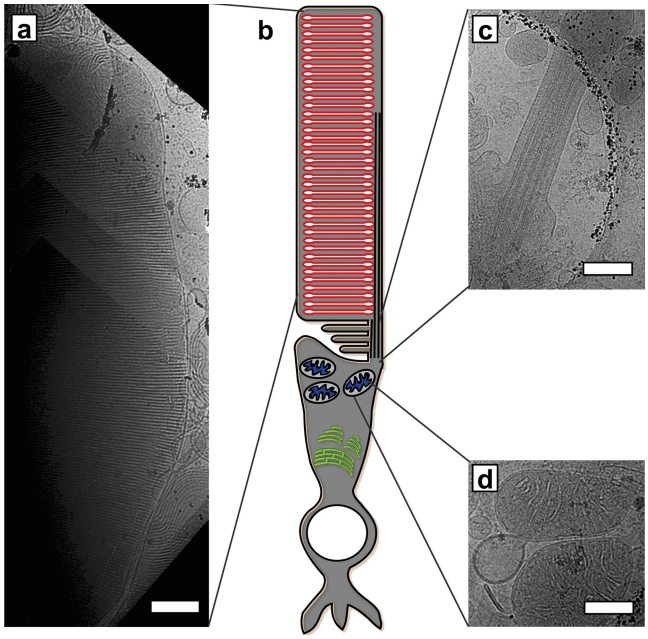

Figure 1. **Cryoelectron micrograph of a vitrified ROS.** Photoreceptor cells, schematically shown in panel b, are highly differentiated cells with a cylindrical ROS. (a) Montage of five cryoelectron micrographs of a single ROS. The reduced thickness of the ROS on the right side allows for a clear image of stacked discs and the plasma membrane. (c and d) Other components of photoreceptor cells such as connecting cilia (c) and mitochondria (d) are also found on EM grids. Bars (a), 500 nm; (c and d) 400 nm.

among vertebrate ROS structures. The diameter of discs, number of stacked discs, and length of the ROS is much greater in amphibians (e.g., frogs and mudpuppies) compared with mammals. The number and depth of incisures, which are invaginations at the periphery of discs, is also variable among species. Rodent and bovine discs display only a single incisure, whereas amphibian discs can have as many as 30 deeply penetrating incisures (Wald et al., 1963; Rosenkranz, 1977; Papermaster et al., 1978).

Dimensions of the interior space of the ROS have been determined from EM studies for many different species (Table I). Reports from the frog are by far the most abundant. Measurements for murine photoreceptors are not present in the literature. Variations are observed among measurements obtained for the same species, which may reflect differences that can arise from preparatory demands inherent to EM methods. Accurate measurements for the dimension of the intricate membrane system within the ROS are necessary to provide a proper framework in which to carry out theoretical studies on phototransduction (Lamb and Pugh, 1992; Andreucci et al., 2003; Holcman and Korenbrot, 2004).

In this study, cryoelectron tomography (ET [cryo-ET]) was used to visualize the detailed morphology of the ROS from the retina of mice in three dimensions. Cryo-ET combines optimal structure preservation with the advantage of three-dimensional imaging (Dubochet et al., 1988; Grunewald et al., 2003; Nickell et al., 2006). Tomograms of vitrified samples of the ROS revealed the existence of spacer structures connecting adjacent discs at locations not observed previously in the ROS of other species. The distances between the membranes comprising the ROS were determined from micrographs to provide an accurate framework for the space within which phototransduction occurs.

Results

Highly enriched and structurally preserved ROS preparations were obtained from murine retina as described previously (Liang et al., 2003). Samples of purified ROS were vitrified by rapid freezing in liquid ethane. Micrographs of vitrified samples displayed characteristic features of the ROS (Fig. 1 a). The organization of discs exhibited a high degree of order (Fig. 2). Other organelles such as the cilium that connects the ROS to the rod inner segment and mitochondria that reside in the rod inner segment also were detected in some micrographs (Fig. 1, c and d).

Multiple single-axis tilt series were recorded of vitrified samples of ROS (Video 1, available at http://www.jcb.org/cgi/content/full/jcb.200612010/DC1) to compute three-dimensional reconstructions (representative tomograms of a ROS are shown in Figs. 3 and S1). An isosurface representation of the ROS was created from the reconstructed tomogram to provide a three-dimensional view of the structure (Figs. 4 and S2). Distance measurements between different membrane structures in the ROS recorded from cryoelectron tomograms are illustrated in Fig. 5 and reported in Table I. Mean distance measurements were obtained from three datasets and were consistent among the different datasets.

The volume of the ROS cytoplasm and a single disc was calculated based on measurements determined from cryoelectron tomograms (Table II). The mean length and diameter of murine ROS have been estimated to be 23.8 μm and 1.32 μm, respectively, and each ROS contains a mean of 810 discs (Liang et al., 2004). The interior volume of a ROS was calculated to be 32×10^{-12} ml. This interior space will be occupied by the cytoplasm and discs. The volumes of the intradisc space and disc membranes were calculated to be 5×10^{-15} ml and 22×10^{-15} ml, respectively. Each disc occupies 27×10^{-15} ml of space, and all discs together will occupy 22×10^{-12} ml of space in the ROS. The cytoplasm occupies the remaining 10×10^{-12} ml of space in the ROS. The cytoplasm in murine ROS represents 31% of the space inside a ROS. This value is lower than the estimated 50% occupancy of amphibian ROS by the cytoplasm (Peet et al., 2004).

The density of disc membranes was not uniform in tomograms (Fig. 4 b), exhibiting areas of high density (Fig. 4 B, dark yellow) and areas of low density (Fig. 4 B, light yellow). The high density regions represented 71% of the disc volume, whereas the low density regions represented the remaining 29% of the disc volume (Fig. 6). The difference in density likely arises from the nonuniform distribution of rhodopsin, which accounts for 90% of all proteins in discs (Filipek et al., 2003; Palczewski, 2006) in disc membranes. Each murine retina has been estimated to contain 6.4×10^6 rod photoreceptor cells (Jeon et al., 1998) and 527 pmol of rhodopsin (Liang et al., 2004). Thus, the total calculated volumes of disc membranes and the ROS cytoplasm in the retina will be 114×10^{-6} ml and 64×10^{-6} ml, respectively. Rhodopsin is then present at a concentration of 4.62 mM in disc

Table I. **Distances between ROS membrane components**

Species	Disc	Single disc membrane	Intradisc space	Interdisc space	Disc–disc	Rim, outer diameter	Distances between rims	PM	Disc-PM	References
	nm	*nm*	*nm*	*nm*	*nm*	*nm*	*nm*	*nm*	*nm*	
Published distances										
Chick	18–23	8	2	ND	29–30	22	6	ND	ND	Godfrey, 1973; Corless et al., 1987a
Cow	9–20	3–6	3–5	6	12–15 (31)[a]	21	ND	ND	ND	Wolken, 1957; Gras and Worthington, 1969; Krebs and Kuhn, 1977; Tonosaki et al., 1980
Frog	12–21 (15)[a]	6–8 (7)[a]	0–2 (0.5)[a]	5–12	22–32 (23–37)[a]	17–26	3–8	7–8	ND	Wolken, 1957; Moody and Robertson, 1960; Nilsson, 1965; Cohen, 1968; Blaurock and Wilkins, 1969, 1972; Gras and Worthington, 1969; Corless, 1972; Webb, 1972; Korenbrot et al., 1973; Nir and Pease, 1973, 1975; Nir and Hall, 1974; Usukura and Yamada, 1981; Corless et al., 1987a
Guinea pig	6–28	3–9	0–10	4–20	10–48	ND	ND	ND	ND	Sjostrand, 1949, 1953; Finean et al., 1953; Clark and Branton, 1968
Human	22.5	6.5	9.5	10	32.5	ND	ND	ND	ND	Missotten, 1964
Monkey	15–20	4	7–12	11	32	ND	ND	5	ND	Cohen, 1961; Dowling, 1965
Mudpuppy	10–14	5	0–4	15	27	ND	ND	ND	ND	Brown et al., 1963; Wald et al., 1963
Perch	24	8	8	8	32	ND	ND	ND	ND	Finean et al., 1953; Sjostrand, 1953
Pigeon	11–13	ND	ND	14–18	27–28	ND	ND	ND	ND	Cohen, 1963
Rabbit	10–13	4–7	0–2	11–30	19–24	ND	ND	ND	ND	De Robertis and Lasansky, 1958; Sjostrand and Nilsson, 1964; Townes-Anderson et al., 1988
Rat	ND	8–9	ND	ND	(33)[a]	ND	ND	ND	ND	Gras and Worthington, 1969; Leeson, 1970
Squirrel	13	ND	ND	ND	22	ND	ND	ND	ND	Cohen, 1964
Toad	11	4	3	5	16	ND	ND	ND	ND	Lasansky and De Robertis, 1960
Distances from this study[b]										
Mouse	21 ± 1	8 ± 1	4 ± 1	14 ± 3	35[c]	26 ± 2	7 ± 1	7 ± 1	17 ± 4	This study

PM, plasma membrane. Measured distances (A–I) from this study are illustrated in Fig. 5: A, disc; B, single disc membrane; C, intradisc space; D, interdisc space; E, disc–disc; F, rim, outer diameter; G, distances between rims; H, plasma membrane; I, disc–plasma membrane.

[a]Values in parentheses were derived from x-ray diffraction studies.

[b]Mean distances are shown with the SD. Distances were measured from three data sets. A total of 50 positions were measured to compute each mean. The number of positions measured in each data set is as follows: 20, 15, and 15. To increase the signal to noise ratio, a mean over 10 neighboring pixels was calculated perpendicular to the segment at each position.

[c]Value was calculated from measured distances of A (disc) and D (interdisc space).

membranes and at a concentration of 8.23 mM with respect to the ROS cytoplasm. The density of rhodopsin in the disc membrane is estimated to be 24,102 molecules/μm^2 on average or up to ~34,000 molecules/μm^2 in high density patches.

The isosurface representation of tomograms also revealed spacer structures that connect discs to the plasma membrane and to adjacent discs (Fig. 4). The spacers between adjacent discs were seen not only at the rim region but also at the lamellar regions of the discs. Such spacers were distributed throughout the discs at a mean density of 492 ± 134 molecules/μm^2 (n = 18). The size of spacers was heterogeneous, and they had a mean estimated mass of 500 ± 100 kD. This mass was calculated by determining the mean volume of 125 spacers and assuming a protein density of 1.3 g/cm^3. The missing information in Fourier space as the result of a limited tilt range of specimens (i.e., missing wedge; Lucic et al., 2005) was not taken into account in the calculation of the mass of spacers. Spacers were observed independent of the orientation of the missing wedge.

Discussion

The challenge in studying the ultrastructure of the ROS is the preservation of the native state of the membrane structure and of macromolecules. This challenge is reflected in the variations observed in distance measurements between membrane structures of the ROS obtained from conventional EM studies (Table I).

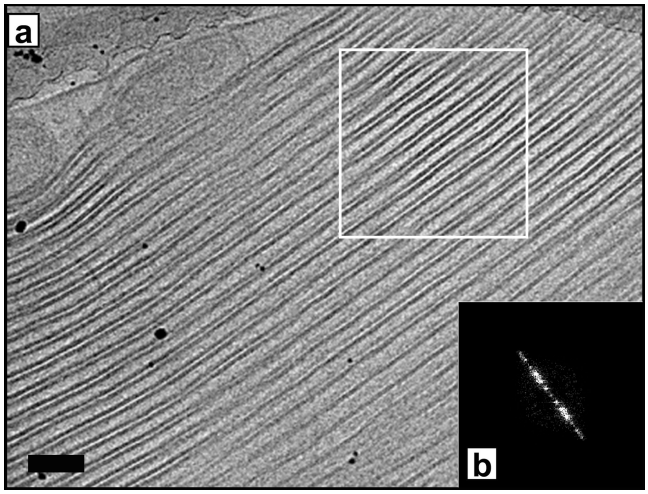

Figure 2. **Highly ordered disc membranes in vitrified ROS.** (a) Cryoelectron micrograph of stacked disc membranes. A single transmission projection was obtained at a defocus value of −10 μm. The diffraction spectrum was obtained from the region highlighted by the boxed area. (b) The high order of discs is reflected in the diffraction spectrum. Up to five maxima are distinguishable. Bar, 100 nm.

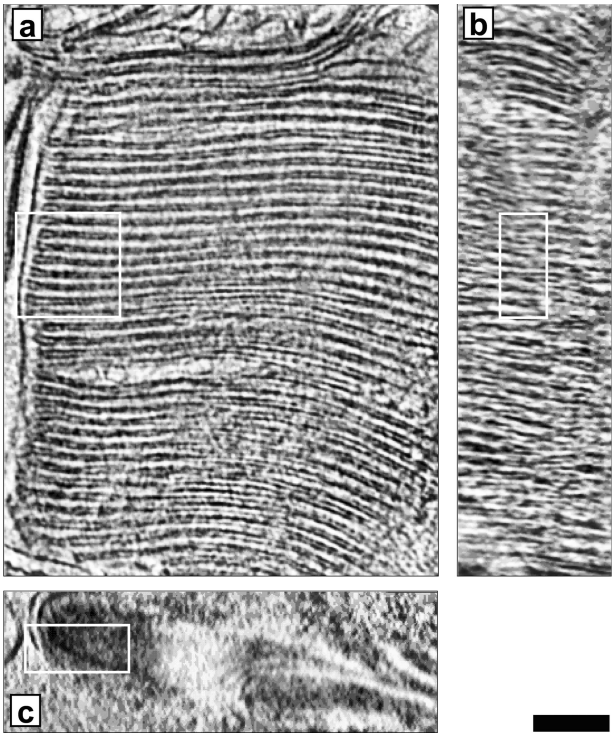

Figure 3. **Electron tomogram of vitrified ROS.** The electron tomogram is represented in three orthogonal slices through the volume of the ROS. (a and b) An x-y slice (a) and a y-z slice (b) display the high order and regular arrangement of stacked discs. (c) A x-z slice shows the high concentration of rhodopsin found in disc membranes. The reconstruction was not binned, and the pixel size is 1.1 nm. The boxed areas are visualized by isosurface representation in Fig. 4. Bar, 200 nm.

The reported measurements were variable even for the same species, which highlights the risk of artifacts associated with conventionally prepared samples that can compromise the reliability of quantifications. In transmission EM (TEM) studies, samples are often chemically fixed, dehydrated, embedded, sectioned, and heavy metal stained, which can introduce artifacts (Rosenkranz, 1970). The osmolarity of buffers used at various stages of sample preparation as well as the dehydration required for plastic embedding can have considerable effects on distances between disc membranes (Heller et al., 1971; Blaurock and Wilkins, 1972; Falk and Fatt, 1973; Korenbrot et al., 1973). Also, the choice of fixatives and stains can alter the structure and dimensions of membranes in the ROS (Cohen, 1963; Godfrey, 1973; Nir and Pease, 1975). Freeze fracture or freeze etch studies avoid some of the problems associated with TEM sample preparations. However, samples still undergo some processing, such as fracturing and metal shadowing, which can also result in artifacts and difficulties in obtaining accurate quantitative data (Clark and Branton, 1968).

Cryo-ET avoids most of the potential pitfalls associated with conventional EM preparatory steps because blotting and vitrification are the only processing steps that samples are subjected to. Thus, preparatory steps in cryo-ET are minimally invasive. Vitrification aids in the preservation of the native state of macromolecules because vitrified water is amorphous in character like liquid water and keeps samples hydrated (Dubochet et al., 1988). Despite these advances over conventional EM methods, cryo-ET is not free from all potential sources of the native state disruption of samples. Cells and lipid vesicles studied by cryo-ET undergo varying degrees of compression that may arise from the capillary forces introduced during the blotting procedure (Dierksen et al., 1995; Grimm et al., 1996, 1998; Frangakis et al., 2002; Nickell et al., 2003). The compression of samples reduces the thickness of samples and can result in the collapse of the cell structure in some instances (Grimm et al., 1998).

The murine ROS represents one of the largest structures to be studied by cryo-ET so far. ROS from mice have a diameter of 0.85–1.4 μm (Liang et al., 2003, 2004), which places this structure at the size limit for study by cryo-ET without sectioning. The ROS appears to undergo some compression, as indicated in Fig. 1 a, where the left half of the ROS is obscured as a result of the thickness of the sample in that area. Compression of discs may lead to breakage at one edge in some instances (Fig. S3, available at http://www.jcb.org/cgi/content/full/jcb.200612010/DC1). The high degree of order exhibited by discs, the consistency of quantitative measurements, and the conservation of features highlighted in this study among all datasets analyzed suggest that the native state of the ROS in analyzed datasets has been preserved in large part.

Measurements of distances between membranes of the ROS obtained in this study are similar to some of the reported values obtained from other species, including amphibians (Table I). Distances between adjacent discs and between disc rims and the plasma membrane may be conserved across all species. The thickness of a single disc membrane measured from cryo-ET micrographs is the same as that determined from atomic force microscopy (AFM) studies on murine ROS discs (Fotiadis et al., 2003; Liang et al., 2003) and bovine ROS discs (Sapra et al., 2006). Similar to cryo-ET, AFM imaging in buffer solution allows for studies on samples in a near-native state. The thickness of a single disc membrane was 8 nm from cryo-ET images.

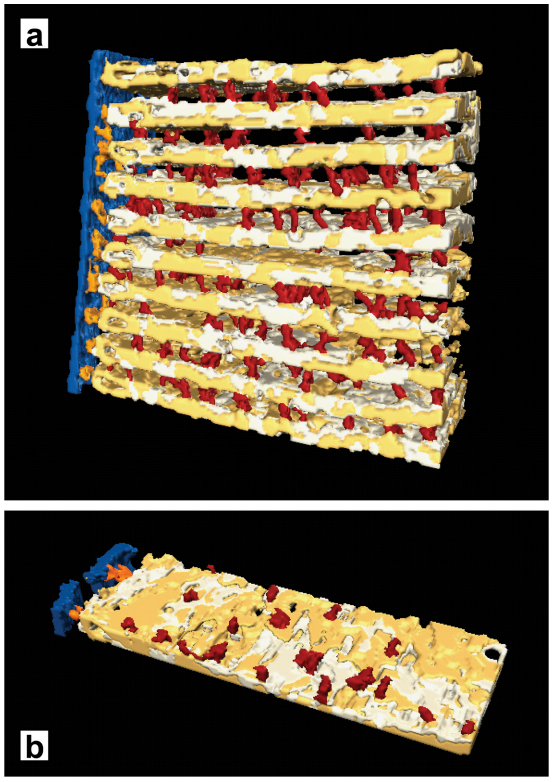

Figure 4. **Isosurface representation of a ROS.** (a) A subvolume containing 10 discs (yellow) and the plasma membrane (blue) are shown. Areas of high density (dark yellow), presumably rhodopsin, can be differentiated from less dense areas (light yellow). (b) A top view of a single disc is shown. Spacers are shown that connect adjacent discs to each other (red) and the rim region of discs to the plasma membrane (orange).

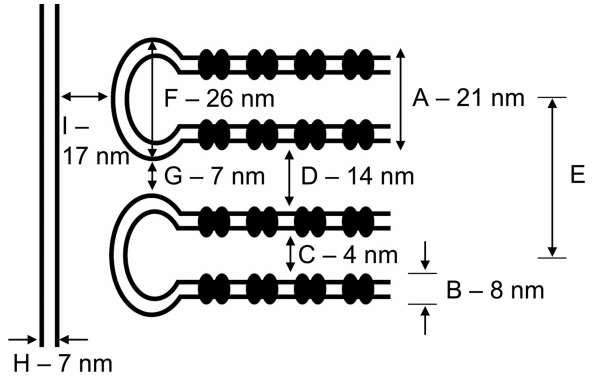

Figure 5. **Measured distances between ROS membrane components.** A schematic of a plasma membrane and two discs is shown. The measured distances between membrane components listed in Table I are illustrated on the schematic.

This thickness likely derives from the length of rhodopsin molecules rather than lipids because a lipid bilayer devoid of proteins is typically ∼4 nm in thickness (Liang et al., 2003; Sapra et al., 2006). The agreement of cryo-ET data with AFM data demonstrates the reliability of measurements made from cryo-ET micrographs.

Tomographic reconstructions provide three-dimensional information about the ROS structure (Figs. 3 and 4). The interplay between electron dose and the level of noise that accompanies the signal sets the resolution limit in cryo-ET (Henderson, 2004; Lucic et al., 2005). Radiation damage of the specimen limits the electron dose, which leads to low contrast and a low signal to noise ratio in tomograms. The tomograms analyzed contain information up to the resolution limit of ∼3–5 nm, which is determined by the instrumentation and reconstruction procedure. However, the resolution in ROS tomograms will be lower than the resolution limit because of the noise level.

The resolution of tomograms was not sufficient to detect individual rhodopsin molecules in the disc membrane. The nonuniform density of the disc membranes suggests that rhodopsin is heterogeneously distributed in the membrane (Fig. 6). Regions that display no density are also present in the disc membrane. These areas are indistinguishable from the density of the surrounding buffer solution and may represent holes in the membrane. The nature of these density-free regions requires further investigation.

Rhodopsin, like other G protein–coupled receptors, likely form dimers or higher order oligomers (Park et al., 2004; Kota et al., 2006; Mansoor et al., 2006). AFM measurements and power spectra recorded from TEM micrographs of negatively stained isolated disc membranes suggest that rhodopsin oligomers can exist in paracrystalline arrays (Fotiadis et al., 2003; Liang et al., 2003). In contrast, power spectra measured from discs in tomograms of the ROS gave no indication of a paracrystalline arrangement of rhodopsin. The propensity of rhodopsin to form paracrystalline arrays under native conditions and the proportion of discs within a ROS that display this arrangement requires further investigation.

The rim region of discs can maintain contact with the plasma membrane and proper spacing along the length of the ROS even in the absence of the lamellar region of discs destroyed either by osmotic pressure or treatment with osmium tetroxide and Tris (Falk and Fatt, 1969; Cohen, 1971). Sporadic reports have been made of spacer structures connecting adjacent discs and connecting the rim region of discs to the plasma membrane in EM micrographs of ROS from species including the frog, toad, eel, rabbit, cow, and rat (Usukura and Yamada, 1981; Roof and Heuser, 1982; Corless and Schneider, 1987; Corless et al., 1987b; Townes-Anderson et al., 1988; Miyaguchi et al., 1992; Kajimura et al., 2000). Spacers reported in these studies were localized mainly to the rim region and incisures of discs and may play a role in anchoring the rim region of discs in their position. Such spacers are sensitive to the fixation procedures, and their presence seems to depend on the preparatory procedures used (Corless et al., 1987b; Townes-Anderson et al., 1988). Spacers appear to be flexible and can be stretched up to 30 nm before breaking (Roof and Heuser, 1982). Spacers connecting the rim region of discs to the plasma membrane appear to have different characteristics compared with those connecting adjacent discs (Roof and Heuser, 1982; Miyaguchi et al., 1992; Kajimura et al., 2000).

Lamellar regions of discs are flexible and prone to deformations. Reports of spacer structures in this region are largely absent. In the few instances in which such structures were observed, they occurred less frequently than those found at the rim region (Usukura and Yamada, 1981; Roof and Heuser, 1982).

Table II. **Quantitative parameters for murine ROS**

Parameter description	Parameter value
Mean length of ROS	23.8 μm[a]
Mean diameter of ROS	1.32 μm[a]
Mean diameter of disc	1.27 μm
Mean number of discs per ROS	810[a]
Number of ROS per eye	6.4×10^{6}[b]
Amount of rhodopsin per eye	527 pmol[a]
Total interior volume of ROS (cytoplasm volume + total disc volume)	32×10^{-12} mL
Volume of intradisc space (single disc)	5×10^{-15} mL
Volume of disc membranes (single disc)	22×10^{-15} mL
Volume of ROS cytoplasm	10×10^{-12} mL
Surface area of single disc membrane	1.27 μm^2
Concentration of rhodopsin in disc membrane	8.23 mM
Density of rhodopsin in disc membrane	24,102 molecules/μm^2
Density of spacers in disc membrane[c]	492 molecules/μm^2

[a]Value obtained from Liang et al. (2004).
[b]Value obtained from Jeon et al. (1998).
[c]The mean density of spacers was determined from two data sets and a sampling of 18 discs.

In contrast, our tomograms of the ROS display spacer structures linking adjacent discs to be distributed throughout the disc rather than concentrated at the periphery of the disc (Fig. S4, available at http://www.jcb.org/cgi/content/full/jcb.200612010/DC1). Part of the difference between our results and those reported by others may relate to variability in the number and depth of incisures observed among different species. Most studies have been performed in frogs, in which the discs have many incisures that constitute a large surface area. On the other hand, discs from mice have only a single incisure (Cohen, 1960). If spacers were localized exclusively in the rim region and in the incisures of discs in mice, the large lamellar area would be without the proper support to maintain the precise stacking of the discs. Spacers may be distributed throughout the disc surface from murine ROS to facilitate the absence of a large number of deeply penetrating incisures. Alternatively, spacers connecting the lamellar regions of adjacent discs may be more susceptible to disruption by conventional EM preparatory steps and, therefore, have gone undetected, for the most part, until now because of the preservation afforded by vitrification.

The molecular identity of proteins comprising spacer structures is unknown. The spacers are required to span a distance of 14 nm between adjacent discs and 17 nm between the rim region of discs and the plasma membrane. A fairly large macromolecular complex would be needed to provide the bridge between adjacent discs in the lamellar regions with a mass in the range of ~500 kD. The spacers are likely composed of a complex of proteins, and spacers in different regions may have different molecular compositions. The protein or protein complexes that comprise the spacers will be present at a level that is ~49 times less than that of rhodopsin. No structural proteins have been implicated yet in the lamellar region of discs. All characterized structural proteins to date are localized to the disc periphery or incisure regions. Proteins involved in spacer complexes may include peripherin-2 and ROM-1, which are members of the tetraspanin family of proteins. Both proteins have been implicated as structural components required for the maintenance of ROS morphology and disc stacking. The importance of these proteins in maintaining the regular structure of the ROS, peripherin in particular, is revealed in *rds* mice homozygous for the disrupted peripherin gene. Homozygous mice fail to develop ROS, and heterozygous mice produce highly disorganized disc structures (Kedzierski et al., 2001). Peripherin associates through intramolecular and intermolecular disulfide bonds with itself and with ROM-1 to form a mixture of homo- and heterotetramers (Goldberg and Molday, 2000; Loewen and Molday, 2000).

Rod photoreceptors also contain a set of glutamic acid–rich proteins (GARPs) that may be another component of spacer complexes. EM images show that GARPs appear to be localized in the rim region and incisures of discs in close proximity to guanylate cyclase and ABCR. GARPs have been proposed to organize a dynamic protein complex between the cyclic guanosine monophosphate–gated channels in the plasma membrane and peripherin in the rim region of discs, thereby playing a role

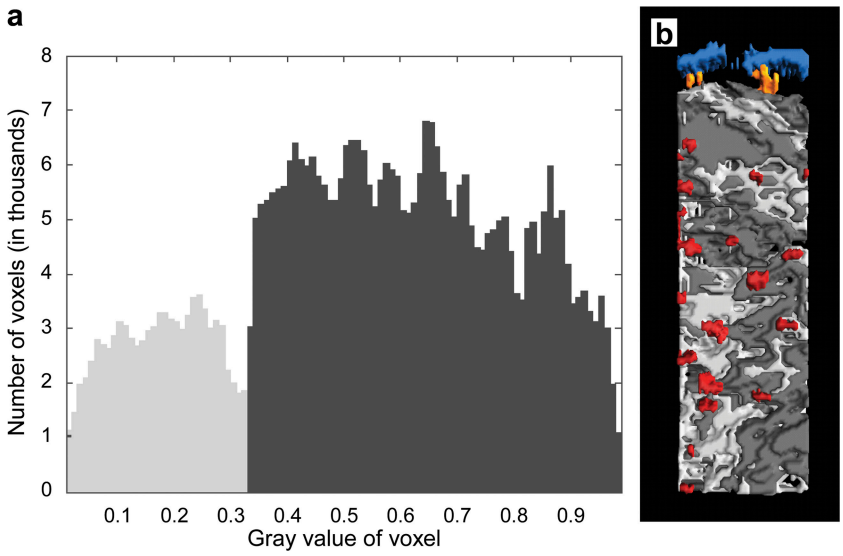

Figure 6. **Histogram of the gray values of disc membranes.** (a) The gray value for each voxel (three-dimensional pixel) in the disc membrane volume was computed for 10 disc samples. Areas of low density (gray value < 0.33; light gray bars) represented 29% of the disc volume, and areas of high density (gray value > 0.33; dark gray bars) represented 71% of the disc volume. (b) The distribution of high (dark gray) and low (light gray) density regions is shown in a top view of a single disc.

in maintaining the distance between the rim region of the disc and the plasma membrane (Korschen et al., 1999; Poetsch et al., 2001). Soluble GARPs have been proposed to form a complex with the peripherin-2–ROM-1 complex to bridge the rim region of adjacent discs (Batra-Safferling et al., 2006). GARPs have been shown to be unstructured and flexible, a feature that would be beneficial for spacer structures to accommodate minor changes in the structure of the discs.

Concluding remarks

This study on murine ROS is a first step in applying cryo-ET to the visual system, and further advancements in this emerging technology will provide even greater details and resolution of this important visual structure. Vitrification of samples allowed visualization of the ROS and disc membranes in a minimally perturbed state without the processing steps involved in conventional EM approaches. Reconstruction of single-axis tilt series images permitted a three-dimensional rendering of a region of the ROS that included the plasma membrane and disc membranes. Spacer structures have been observed that likely play a role in maintaining the ordered spacing between adjacent discs and between discs and the plasma membrane. Precise assignment of distances between various membrane components of the ROS was possible because of the noninvasive and close-to-life state of sample preservation. As a result, a blueprint of the ROS with precise distance measurements has been obtained. This blueprint provides both physical constraints within which phototransduction can occur and a framework within which the organization of proteins can be understood. With such a framework in hand, improved theoretical approaches can be used to obtain more accurate quantitative descriptions of the signaling process (Andreucci et al., 2003; Holcman and Korenbrot, 2004).

Materials and methods

Isolation of ROS from mouse retina

C57BL/6 mice were obtained from The Jackson Laboratory. All procedures were performed under dim red light. Mice were maintained in darkness overnight before being killed. Retinal tissue from 15 mice (~8 wk old) were placed in 300 µl of 8% (vol/vol) OptiPrep (Nycomed) in Ringer's buffer (10 mM Hepes, 130 mM NaCl, 3.6 mM KCl, 2.4 mM $MgCl_2$, 1.2 mM $CaCl_2$, and 0.02 mM EDTA, pH 7.4). The solution was vortexed at maximum speed for 1 min, and the sample was then centrifuged at 238 g_{max} for 1 min. The supernatant was removed and stored on ice. The pellet was resuspended in 300 µl of solution containing 8% OptiPrep in Ringer's buffer, and the vortexing and centrifugation procedure was repeated as described above. This sequence was repeated five times. Supernatant from each spin was pooled and layered on a 10–30% (vol/vol) continuous gradient of OptiPrep in 12 ml of Ringer's buffer. The gradient was centrifuged for 50 min at 26,500 g_{max} and 4°C with no brakes. Intact ROS migrates as a second band about two thirds of the way from the top. Intact ROS was collected and diluted threefold in Ringer's buffer. This suspension was then centrifuged for 3 min at 627 g_{max}. The supernatant was collected and centrifuged for 30 min at 26,500 g_{max}. The resulting pellet contained intact ROS. The pellet was resuspended in 40 µl of Ringer's buffer, and the resulting suspension was used to prepare the EM grids.

ET

An aliquot of ROS was applied to grids covered with holey carbon film pretreated with a mixture of 5–25 nm of gold bead markers. Excess liquid was blotted with filter paper and immediately plunged into liquid ethane (Dubochet et al., 1988). Grids were transferred into liquid nitrogen and mounted on single-tilt cryoholders. ET was performed using a CM300 FEG electron microscope (Philips) and a Tecnai Polara G^2 electron microscope (FEI) working at an accelerating voltage of 300 kV and equipped with a postcolumn energy filter (GIF 2002; Gatan, Inc.) operated in the zero-loss mode. Single-axis tilt series were recorded ranging typically from –65 to 65° with 1–2° increments. Electron micrographs, each covering 2,048 × 2,048 pixels, were recorded at magnifications between 20,000 and 40,000× with a pixel size at the specimen level of 0.5–1.1 nm. The defocus was set to between −4 and −6 µm unless otherwise noted, resulting in a first zero of the phase-contrast transfer function between 3 and 5 nm^{-1}. All tomographic data acquisition steps were performed by fully automated procedures under strict low-dose conditions. Accumulative doses for recording the tilt series were ~40,000–100,000 e/nm^2.

Image processing

All image processing steps were performed using the TOM software toolbox (Nickell et al., 2005). Images of individual tilt series were aligned with each other using colloidal gold beads as marker points added before cryofixation. Markers were picked interactively on a graphics display, and their coordinates were used to compute the alignment parameters. Alignment and three-dimensional reconstruction was performed by weighted backprojection. A total of 10 tomographic datasets were analyzed. Tomograms shown in Figs. 3 and S1 are representative of the datasets analyzed. Visualization and isosurface representations of the tomograms were generated with Amira software (Mercury Computer Systems, Inc.). Individual components found in the isosurface images were segmented manually. The isosurface threshold was determined for each component separately. A mean isosurface value was computed for each component by probing at 20 or more positions. This mean isosurface value was then used as the threshold value.

Online supplemental material

Fig. S1 is an electron tomogram of vitrified ROS obtained from a different dataset than that represented in Fig. 3. Fig. S2 is an isosurface representation of a selected area from the electron tomogram of a ROS shown in Fig. S1. Fig. S3 is a cryoelectron micrograph showing compressed ROS discs. Fig. S4 is a schematic showing the distribution of spacers in discs. Video 1 shows a single-axis tilt series for a ROS. Video 2 shows an electron tomogram and isosurface representation of a ROS. Online supplemental material is available at http://www.jcb.org/cgi/content/full/jcb.200612010/DC1.

We would like to acknowledge Dr. Yan Liang for her contributions to initial stages of this study.

This work was supported by National Institutes of Health grants EY08061, EY017004, and EY018085 and by a grant from Amgen, Inc. P.S.-H. Park is the recipient of postdoctoral fellowships from the Natural Sciences and Engineering Council of Canada and the Foundation Fighting Blindness (Canada).

Submitted: 4 December 2006
Accepted: 3 May 2007

References

Andreucci, D., P. Bisegna, G. Caruso, H.E. Hamm, and E. DiBenedetto. 2003. Mathematical model of the spatio-temporal dynamics of second messengers in visual transduction. *Biophys. J.* 85:1358–1376.

Arshavsky, V.Y., T.D. Lamb, and E.N. Pugh Jr. 2002. G proteins and phototransduction. *Annu. Rev. Physiol.* 64:153–187.

Batra-Safferling, R., K. Abarca-Heidemann, H.G. Korschen, C. Tziatzios, M. Stoldt, I. Budyak, D. Willbold, H. Schwalbe, J. Klein-Seetharaman, and U.B. Kaupp. 2006. Glutamic acid-rich proteins of rod photoreceptors are natively unfolded. *J. Biol. Chem.* 281:1449–1460.

Batten, M.L., Y. Imanishi, D.C. Tu, T. Doan, L. Zhu, J. Pang, L. Glushakova, A.R. Moise, W. Baehr, R.N. Van Gelder, et al. 2005. Pharmacological and rAAV gene therapy rescue of visual functions in a blind mouse model of Leber congenital amaurosis. *PLoS Med.* 2:e333.

Blaurock, A.E., and M.H. Wilkins. 1969. Structure of frog photoreceptor membranes. *Nature*. 223:906–909.

Blaurock, A.E., and M.H. Wilkins. 1972. Structure of retinal photoreceptor membranes. *Nature*. 236:313–314.

Brown, P.K., I.R. Gibbons, and G. Wald. 1963. The visual cells and visual pigment of the mudpuppy, Necturus. *J. Cell Biol.* 19:79–106.

Chang, B., N.L. Hawes, R.E. Hurd, M.T. Davisson, S. Nusinowitz, and J.R. Heckenlively. 2002. Retinal degeneration mutants in the mouse. *Vision Res.* 42:517–525.

Clark, A.W., and D. Branton. 1968. Fracture faces in frozen outer segments from the guinea pig retina. *Z. Zellforsch. Mikrosk. Anat.* 91:586–603.

Cohen, A.I. 1960. The ultrastructure of the rods of the mouse retina. *Am. J. Anat.* 107:23–48.

Cohen, A.I. 1961. The fine structure of the extrafoveal receptors of the Rhesus monkey. *Exp. Eye Res.* 1:128–136.

Cohen, A.I. 1963. The fine structure of the visual receptors of the pigeon. *Exp. Eye Res.* 2:88–97.

Cohen, A.I. 1964. Some observations on the fine structure of the retinal receptors of the American gray squirrel. *Invest. Ophthalmol.* 3:198–216.

Cohen, A.I. 1968. New evidence supporting the linkage to extracellular space of outer segment saccules of frog cones but not rods. *J. Cell Biol.* 37:424–444.

Cohen, A.I. 1971. Electron microscope observations on form changes in photoreceptor outer segments and their saccules in response to osmotic stress. *J. Cell Biol.* 48:547–565.

Corless, J.M. 1972. Lamellar structure of bleached and unbleached rod photoreceptor membranes. *Nature*. 237:229–231.

Corless, J.M., and T.G. Schneider. 1987. Patterns of interdisk connections within the lamellar domains of retinal rod outer segment disks: observations relevant to the axial propagation of incisures. *Exp. Eye Res.* 45:883–905.

Corless, J.M., R.D. Fetter, and M.J. Costello. 1987a. Structural features of the terminal loop region of frog retinal rod outer segment disk membranes: I. Organization of lipid components. *J. Comp. Neurol.* 257:1–8.

Corless, J.M., R.D. Fetter, O.B. Zampighi, M.J. Costello, and D.L. Wall-Buford. 1987b. Structural features of the terminal loop region of frog retinal rod outer segment disk membranes: II. Organization of the terminal loop complex. *J. Comp. Neurol.* 257:9–23.

Daemen, F.J. 1973. Vertebrate rod outer segment membranes. *Biochim. Biophys. Acta*. 300:255–288.

Dalke, C., and J. Graw. 2005. Mouse mutants as models for congenital retinal disorders. *Exp. Eye Res.* 81:503–512.

De Robertis, E., and A. Lasansky. 1958. Submicroscopic organization of retinal cones of the rabbit. *J. Biophys. Biochem. Cytol.* 4:743–746.

Dejneka, N.S., T.S. Rex, and J. Bennett. 2003. Gene therapy and animal models for retinal disease. *Dev. Ophthalmol.* 37:188–198.

Dierksen, K., D. Typke, R. Hegerl, J. Walz, E. Sackmann, and W. Baumeister. 1995. Three-dimensional structure of lipid vesicles embedded in vitreous ice and investigated by automated electron tomography. *Biophys. J.* 68:1416–1422.

Dowling, J.E. 1965. Foveal receptors of the monkey retina: fine structure. *Science*. 147:57–59.

Dubochet, J., M. Adrian, J.J. Chang, J.C. Homo, J. Lepault, A.W. McDowall, and P. Schultz. 1988. Cryo-electron microscopy of vitrified specimens. *Q. Rev. Biophys.* 21:129–228.

Falk, G., and P. Fatt. 1969. Distinctive properties of the lamellar and disk-edge structures of the rod outer segment. *J. Ultrastruct. Res.* 28:41–60.

Falk, G., and P. Fatt. 1973. Changes in structure of the disks of retinal rods in hypotonic solutions. *J. Cell Sci.* 13:787–797.

Filipek, S., R.E. Stenkamp, D.C. Teller, and K. Palczewski. 2003. G protein-coupled receptor rhodopsin: a prospectus. *Annu. Rev. Physiol.* 65:851–879.

Finean, J.B., F.S. Sjostrand, and E. Steinmann. 1953. Submicroscopic organisation of some layered lipoprotein structures (nerve myelin, retinal rods, and chloroplasts). *Exp. Cell Res.* 5:557–559.

Fotiadis, D., Y. Liang, S. Filipek, D.A. Saperstein, A. Engel, and K. Palczewski. 2003. Atomic-force microscopy: Rhodopsin dimers in native disc membranes. *Nature*. 421:127–128.

Frangakis, A.S., J. Bohm, F. Forster, S. Nickell, D. Nicastro, D. Typke, R. Hegerl, and W. Baumeister. 2002. Identification of macromolecular complexes in cryoelectron tomograms of phantom cells. *Proc. Natl. Acad. Sci. USA*. 99:14153–14158.

Godfrey, A.J. 1973. A study of the ultrastructure of visual cell outer segment membranes. *J. Ultrastruct. Res.* 43:228–246.

Goldberg, A.F., and R.S. Molday. 2000. Expression and characterization of peripherin/rds-rom-1 complexes and mutants implicated in retinal degenerative diseases. *Methods Enzymol.* 316:671–687.

Gras, W.J., and C.R. Worthington. 1969. X-ray analysis of retinal photoreceptors. *Proc. Natl. Acad. Sci. USA*. 63:233–238.

Grimm, R., D. Typke, M. Barmann, and W. Baumeister. 1996. Determination of the inelastic mean free path in ice by examination of tilted vesicles and automated most probable loss imaging. *Ultramicroscopy*. 63:169–179.

Grimm, R., H. Singh, R. Rachel, D. Typke, W. Zillig, and W. Baumeister. 1998. Electron tomography of ice-embedded prokaryotic cells. *Biophys. J.* 74:1031–1042.

Grunewald, K., O. Medalia, A. Gross, A.C. Steven, and W. Baumeister. 2003. Prospects of electron cryotomography to visualize macromolecular complexes inside cellular compartments: implications of crowding. *Biophys. Chem.* 100:577–591.

Heller, J., T.J. Ostwald, and D. Bok. 1971. The osmotic behavior of rod photoreceptor outer segment discs. *J. Cell Biol.* 48:633–649.

Henderson, R. 2004. Realizing the potential of electron cryo-microscopy. *Q. Rev. Biophys.* 37:3–13.

Holcman, D., and J.I. Korenbrot. 2004. Longitudinal diffusion in retinal rod and cone outer segment cytoplasm: the consequence of cell structure. *Biophys. J.* 86:2566–2582.

Jeon, C.J., E. Strettoi, and R.H. Masland. 1998. The major cell populations of the mouse retina. *J. Neurosci.* 18:8936–8946.

Kajimura, N., Y. Harada, and J. Usukura. 2000. High-resolution freeze-etching replica images of the disk and the plasma membrane surfaces in purified bovine rod outer segments. *J. Electron Microsc. (Tokyo)*. 49:691–697.

Kedzierski, W., S. Nusinowitz, D. Birch, G. Clarke, R.R. McInnes, D. Bok, and G.H. Travis. 2001. Deficiency of rds/peripherin causes photoreceptor death in mouse models of digenic and dominant retinitis pigmentosa. *Proc. Natl. Acad. Sci. USA*. 98:7718–7723.

Korenbrot, J.I., D.T. Brown, and R.A. Cone. 1973. Membrane characteristics and osmotic behavior of isolated rod outer segments. *J. Cell Biol.* 56:389–398.

Korschen, H.G., M. Beyermann, F. Muller, M. Heck, M. Vantler, K.W. Koch, R. Kellner, U. Wolfrum, C. Bode, K.P. Hofmann, and U.B. Kaupp. 1999. Interaction of glutamic-acid-rich proteins with the cGMP signalling pathway in rod photoreceptors. *Nature*. 400:761–766.

Kota, P., P.J. Reeves, U.L. Rajbhandary, and H.G. Khorana. 2006. Opsin is present as dimers in COS1 cells: identification of amino acids at the dimeric interface. *Proc. Natl. Acad. Sci. USA*. 103:3054–3059.

Krebs, W., and H. Kuhn. 1977. Structure of isolated bovine rod outer segment membranes. *Exp. Eye Res.* 25:511–526.

Lamb, T.D., and E.N. Pugh Jr. 1992. A quantitative account of the activation steps involved in phototransduction in amphibian photoreceptors. *J. Physiol.* 449:719–758.

Lasansky, A., and E. De Robertis. 1960. Electron microscopy of retinal photoreceptors. The use of chromation following formaldehyde fixation as a complementary technique to osmium tetroxide fixation. *J. Biophys. Biochem. Cytol.* 7:493–498.

Leeson, T.S. 1970. Rat retinal rods: freeze-fracture replication of outer segments. *Can. J. Ophthalmol.* 5:91–107.

Liang, Y., D. Fotiadis, S. Filipek, D.A. Saperstein, K. Palczewski, and A. Engel. 2003. Organization of the G protein-coupled receptors rhodopsin and opsin in native membranes. *J. Biol. Chem.* 278:21655–21662.

Liang, Y., D. Fotiadis, T. Maeda, A. Maeda, A. Modzelewska, S. Filipek, D.A. Saperstein, A. Engel, and K. Palczewski. 2004. Rhodopsin signaling and organization in heterozygote rhodopsin knockout mice. *J. Biol. Chem.* 279:48189–48196.

Loewen, C.J., and R.S. Molday. 2000. Disulfide-mediated oligomerization of Peripherin/Rds and Rom-1 in photoreceptor disk membranes. Implications for photoreceptor outer segment morphogenesis and degeneration. *J. Biol. Chem.* 275:5370–5378.

Lucic, V., F. Forster, and W. Baumeister. 2005. Structural studies by electron tomography: from cells to molecules. *Annu. Rev. Biochem.* 74:833–865.

Mansoor, S.E., K. Palczewski, and D.L. Farrens. 2006. Rhodopsin self-associates in asolectin liposomes. *Proc. Natl. Acad. Sci. USA*. 103:3060–3065.

Missotten, L. 1964. Ultrastructure of ocular tissue. *Bull. Soc. Belge Ophtalmol.* 136:3–204.

Miyaguchi, K., C.H. Kuo, N. Miki, and P.H. Hashimoto. 1992. Topography of opsin within disk and plasma membranes revealed by a rapid-freeze deep-etch technique. *J. Neurocytol.* 21:807–819.

Moody, M.F., and J.D. Robertson. 1960. The fine structure of some retinal photoreceptors. *J. Biophys. Biochem. Cytol.* 7:87–92.

Nickell, S., R. Hegerl, W. Baumeister, and R. Rachel. 2003. Pyrodictium cannulae enter the periplasmic space but do not enter the cytoplasm, as revealed by cryo-electron tomography. *J. Struct. Biol.* 141:34–42.

Nickell, S., F. Forster, A. Linaroudis, W.D. Net, F. Beck, R. Hegerl, W. Baumeister, and J.M. Plitzko. 2005. TOM software toolbox: acquisition and analysis for electron tomography. *J. Struct. Biol.* 149:227–234.

Nickell, S., C. Kofler, A.P. Leis, and W. Baumeister. 2006. A visual approach to proteomics. *Nat. Rev. Mol. Cell Biol.* 7:225–230.

Nilsson, S.E. 1965. The ultrastructure of the receptor outer segments in the retina of the leopard frog (Rana Pipiens). *J. Ultrastruct. Res.* 12:207–231.

Nir, I., and M.O. Hall. 1974. The ultrastructure of lipid-depleted rod photoreceptor membranes. *J. Cell Biol.* 63:587–598.

Nir, I., and D.C. Pease. 1973. Ultrastructural aspects of discs in rod outer segments. *Exp. Eye Res.* 16:173–182.

Nir, I., and D.C. Pease. 1975. Substructure in rod photoreceptor membranes. *Anat. Rec.* 182:15–27.

Palczewski, K. 2006. G protein-coupled receptor rhodopsin. *Annu. Rev. Biochem.* 75:743–767.

Papermaster, D.S., B.G. Schneider, M.A. Zorn, and J.P. Kraehenbuhl. 1978. Immunocytochemical localization of a large intrinsic membrane protein to the incisures and margins of frog rod outer segment disks. *J. Cell Biol.* 78:415–425.

Park, P.S.-H., S. Filipek, J.W. Wells, and K. Palczewski. 2004. Oligomerization of G protein-coupled receptors: past, present, and future. *Biochemistry*. 43:15643–15656.

Peet, J.A., A. Bragin, P.D. Calvert, S.S. Nikonov, S. Mani, X. Zhao, J.C. Besharse, E.A. Pierce, B.E. Knox, and E.N. Pugh Jr. 2004. Quantification of the cytoplasmic spaces of living cells with EGFP reveals arrestin-EGFP to be in disequilibrium in dark adapted rod photoreceptors. *J. Cell Sci.* 117:3049–3059.

Poetsch, A., L.L. Molday, and R.S. Molday. 2001. The cGMP-gated channel and related glutamic acid-rich proteins interact with peripherin-2 at the rim region of rod photoreceptor disc membranes. *J. Biol. Chem.* 276:48009–48016.

Polans, A., W. Baehr, and K. Palczewski. 1996. Turned on by Ca^{2+}! The physiology and pathology of Ca^{2+}-binding proteins in the retina. *Trends Neurosci.* 19:547–554.

Roof, D.J., and J.E. Heuser. 1982. Surfaces of rod photoreceptor disk membranes: integral membrane components. *J. Cell Biol.* 95:487–500.

Rosenkranz, J. 1970. On the fine structure of the frog's rod outer segments, observed by the freeze-etching technique. *Z. Zellforsch. Mikrosk. Anat.* 111:228–262.

Rosenkranz, J. 1977. New aspects of the ultrastructure of frog rod outer segments. *Int. Rev. Cytol.* 50:25–158.

Sjostrand, F.S. 1949. An electron microscope study of the retinal rods of the guinea pig eye. *J. Cell. Comp. Physiol.* 33:383–403.

Sjostrand, F.S. 1953. The ultrastructure of the outer segments of rods and cones of the eye as revealed by the electron microscope. *J. Cell. Comp. Physiol.* 42:15–44.

Sjostrand, F.S., and S.E. Nilsson. 1964. The structure of the rabbit retina as revealed by electron microscopy. *In* The Rabbit in Eye Research. J.H. Prince, editor. Charles C. Thomas, Springfield, IL. 449–513.

Tanuj Sapra, K., P.S. Park, S. Filipek, A. Engel, D.J. Muller, and K. Palczewski. 2006. Detecting molecular interactions that stabilize native bovine rhodopsin. *J. Mol. Biol.* 358:255–269.

Tonosaki, A., M. Yamasaki, H. Washioka, and J. Mizoguchi. 1980. Complementary freeze fracture methods applied to cattle disk membranes. *Arch. Histol. Jpn.* 43:115–126.

Townes-Anderson, E., R.F. Dacheux, and E. Raviola. 1988. Rod photoreceptors dissociated from the adult rabbit retina. *J. Neurosci.* 8:320–331.

Usukura, J., and E. Yamada. 1981. Molecular organization of the rod outer segment. A deep-etching study with rapid freezing using unfixed frog retina. *Biomed. Res.* 2:177–193.

Wald, G., P.K. Brown, and I.R. Gibbons. 1963. The problem of visual excitation. *J. Opt. Soc. Am.* 53:20–35.

Webb, N.G. 1972. X-ray diffraction from outer segments of visual cells in intact eyes of the frog. *Nature*. 235:44–46.

Wolken, J.J. 1957. A comparative study of photoreceptors. *Trans. NY Acad. Sci.* 19:315–327.